IEEE Photonics Journal
An IEEE Photonics Society Publication

Open Access

Calibration of an InP-Based Monolithically Integrated Optical Pulse Shaper

Volume 5, Number 6, December 2013

M. S. Tahvili
E. Smalbrugge
X. J. M. Leijtens
M. J. Wale
M. K. Smit
E. A. J. M. Bente

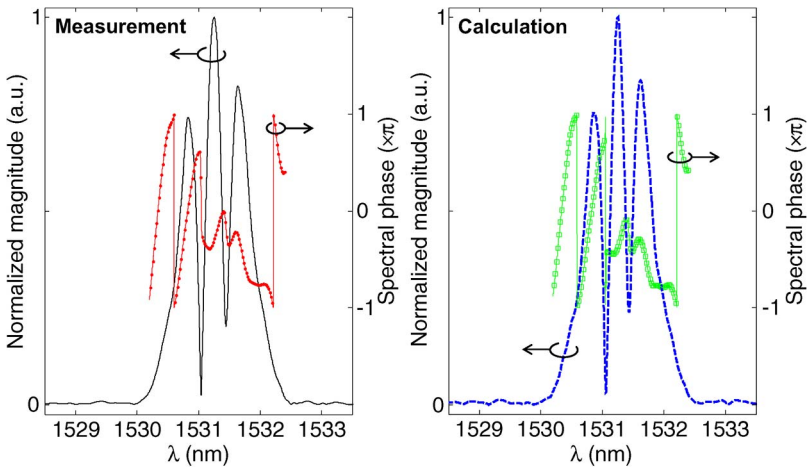

DOI: 10.1109/JPHOT.2013.2289945
1943-0655

Calibration of an InP-Based Monolithically Integrated Optical Pulse Shaper

M. S. Tahvili,[1] E. Smalbrugge,[1] X. J. M. Leijtens,[1] M. J. Wale,[1,2] M. K. Smit,[1] and E. A. J. M. Bente[1]

[1]COBRA Research Institute, Eindhoven University of Technology, 5600MB Eindhoven, The Netherlands
[2]Oclaro Technology Ltd., Caswell, Towcester, NN12 8EQ Northamptonshire, U.K.

DOI: 10.1109/JPHOT.2013.2289945

Manuscript received September 24, 2013; revised October 31, 2013; accepted November 1, 2013. Date of publication November 12, 2013; date of current version November 20, 2013. This work was supported in part by the Technology Foundation STW (Stichting Technische Wetenschappen) and NL Agency of the Dutch Ministry of Economic Affairs and in part by a funding from EU FP7/2007-2013 grant agreement 228839: EuroPIC. Corresponding author: M. S. Tahvili (e-mail: s.tahvili@tue.nl).

Abstract: We present the calibration method and characterization of a monolithically integrated semiconductor optical pulse shaper. The photonic integrated circuit has been realized in an InP-based generic photonic foundry process. In this circuit, a 20-channel arrayed waveguide grating filter with 50-GHz channel spacing and 20 phase modulators and semiconductor optical amplifiers are combined on the InP chip. By calibrating the device, a mathematical description of the pulse shaper is obtained. The theoretical procedure for complete calibration of the device is presented, and the details of the experiments and measurement setups are given. We demonstrate that the frequency response of the pulse shaper can be calculated from the response of the individual channels in a reference state of the control signals and a separate mask function that describes the effect of a change in the control signals.

Index Terms: Integrated optics, optical pulse shaping, photonic integrated circuits, semiconductor device measurement, III-V semiconductors.

1. Introduction

Over the past decades, several optical pulse shaping techniques have been developed and employed for diverse applications. Optical pulse shaping can be defined as manipulation of an (input) optical pulse to synthesize a desired (output) waveform. There are different approaches to achieve pulse shaping, the majority of which are targeted towards specific application requirements. An overview of the progress of pulse shaping techniques and applications is given in [1] and references therein.

Photonic integration technology is capable of providing the required functionalities for building a complex optical system such as an optical pulse shaper. Waveguides, arrayed waveguide gratings (AWGs), phase modulators (PMs), PM-based structures such as interferometers, and semiconductor optical amplifiers (SOAs) are the basic components that are needed to build an integrated circuit which operates as a pulse shaper device. In earlier works, silica-based optical circuits were used to build (partly-) integrated pulse shapers [2]–[4]. More recent attempts include the devices with integrated amplitude and phase modulators [5]–[9] and considerable effort has been directed at development of the InP-based photonic integration platforms for optical pulse shaping [10], [11]. In [12], we have reported on a monolithically integrated optical pulse shaper and demonstrated compression of highly chirped optical pulses generated by a quantum dash mode-locked laser diode.

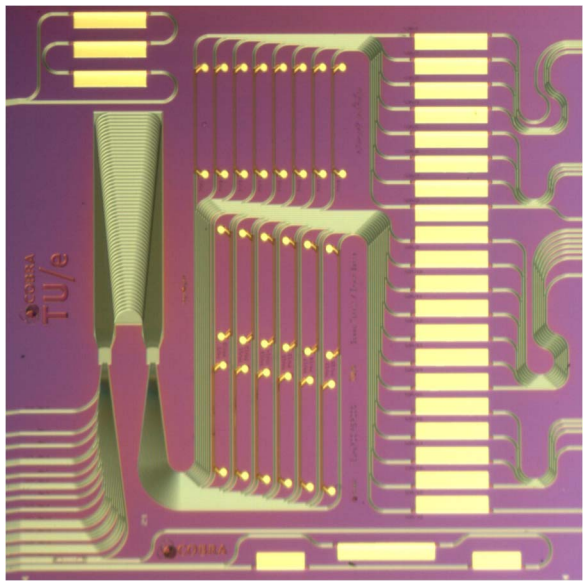

Fig. 1. A microscope image of the realized pulse shaper chip.

In this paper, we present the method and procedure for calibration of the device presented in [12]. An accurate calibration of the device performance and the effect of the device's control signals are required for producing predictable pulse shapes with a shaping device. The paper is organized as follows. We briefly present the realization of the InP-based integrated optical pulse shaper in Section 2. In Section 3, we present the general mathematical description of the Fourier transform pulse shaping technique and the calibration method used. The calibration method is based on defining the frequency response of the device in terms of the frequency response of the individual channels and by describing the effect of control signals on each channel as a mask function. The method is based on a main assumption that the pulse shaper device is a linear time-invariant (LTI) system. This approach has the advantage that the formulated mathematical expressions can be directly related to measurable quantities. In Section 4, we describe how the calibration method is implemented in practice. The measurement setups are presented and the measured results are discussed.

The calibration of the device provides a complete mathematical description of the pulse shaper which is required for operating the device. In Section 5, the channel characterization method is first verified by employing the SIMBA technique. Then a test measurement of the control signal calibration is presented to show that the system response is correctly predicted using the proposed calibration method. The main results are summarized in Section 6 and the paper is concluded.

2. Device Realization and Operation

The device is fabricated in a generic integration technology platform [13], [14] in which the design is based on certain standardized building blocks. In the generic integration platform, the wafer layer stack and fabrication process are optimized for best overall performance and are not tailored towards a specific application. This enables the possibility of multi-user fabrication runs which allow for an earlier (commercial) exploitation of the results. A key advantage of the present platform is the active-passive integration scheme which allows direct integration of active components, such as SOAs with passive elements on a single chip.

A microscope image of the realized chip is presented in Fig. 1. The device has a reflective geometry and includes a single AWG with 20 channels. Each channel has a PM and an SOA. In this design, the AWG is the spectral de-/multiplexer and PMs and SOAs are used to control the phase

and amplitude of the spectral components. The chip size is 6×6 mm^2. The light from the optical pulse source, i.e., a mode-locked (ML) laser, is injected into the pulse shaper chip via an anti-reflection (AR) coated facet (the left hand side facet in Fig. 1). The pulsed signal passes through the AWG which decomposes the light into its spectral components. Each component passes through electro-optic (EO) PMs and SOAs and is then reflected back from a facet with a high-reflection ($\sim$95%) coating (the right hand side facet in Fig. 1). The spectral components are then recombined in the AWG and return through the input/output (I/O) waveguide. The two directions are separated by an optical circulator outside the chip.

The PMs are operated by application of a reverse bias voltage signal and the SOAs are forward biased by a current supply to provide optical gain. The device is mounted on a subcarrier and then glued on a copper block. The operating temperature is controlled using a water cooler that stabilizes the water temperature within 0.1 °C. A thermistor is used to monitor the temperature.

Due to the fact that there is a thermal resistance between the device and the cooling water, the temperature of the device will depend on the amount of heat dissipated in it by the biased SOAs. The temperature dependence of the effective index in the current device has been measured to be approximately $2.5 \times 10^{-4}/°$C which is a typical value for InP waveguides [15]. The device temperature is not automatically stabilized using a thermo-electric cooler element but we operate the pulse shaper at the same constant monitor temperature; we adjust the water temperature such that the temperature sensor indicates 12 ± 0.03 °C.

The length differences between the device channels have been compensated using the extra waveguide sections in the channels. These can be seen in Fig. 1 near the HR-coated facet. Therefore, the optical path length variations due to design inaccuracies (straight vs curved waveguides, etc.) or processing and epitaxial layer growth imperfections, are in practice limited to a few μm. Given the thermal dependence of the effective index, we estimate that the effect of temperature variations on the relative phases of the optical signal passing through the device is less than $\pm 10^{-5}$ rad and negligible.

3. Description of the Calibration Method

The Fourier transform (FT) pulse shaping technique is based on the concept of linear, time-invariant (LTI) systems. Linear systems are generally described in the time domain by an impulse response $h(t)$, and in the frequency domain by $H(\omega)$ which is known as the frequency response. $H(\omega)$ may also be referred to as the system transfer function. $H(\omega)$ is the key to understanding the principle of the FT pulse shaping technique. In a FT pulse shaper, the shape of the output pulse, i.e., the amplitude and phase, is related to the shape of input pulse through the system response of the pulse shaper device as

$$E_{\text{out}}(\omega) = H(\omega) \times E_{\text{in}}(\omega) \tag{1}$$

where E denotes the pulse shape in the frequency domain which is in general complex valued. Eq. (1) implies that the shape of the output pulse can be controlled by manipulating the frequency response of the pulse shaper device.

In a programmable pulse shaper such as the integrated device presented in this paper, the frequency response of the device can be (re-) configured by applying the control signals. This implies that in order to generate predictable pulse shapes, the system requires to be calibrated. Calibration of the pulse shaper in this context is equivalent to finding the frequency response of the pulse shaper device for any condition of the control signals.

In practice, it is not convenient (even possible) to measure the transfer function of a pulse shaper for all the possible combinations of the control signals. Our approach to calibrate the pulse shaper is to identify the system in a "reference" state and consider the effect of control signals separately. The reference state can be defined as any particular set of control signals. This approach is described in more details as follows.

The pulse shaper device consists of several channels. The total response of the pulse shaper is a linear summation of the frequency responses of the operating channels. If the total response of the

system is H_{tot}, we have

$$H_{tot}(\omega, s) = \sum_{i=1}^{N} H_i(\omega, s_i) \tag{2}$$

in which N is the number of channels, H_i is the individual channel response of the channel number i, and s_i stands for the control signals in the corresponding channel. It is convenient to define

$$H_i(\omega, s_i) = HR_i(\omega) \times M_i(s_i) \tag{3}$$

in which $HR_i(\omega)$ is the channel response at the reference state of the control signals. We let the function $M_i(s_i)$ account for the effect of applied control signals on the phase and amplitude of the optical signal in each channel. This means that changes of the phase and amplitude with respect to the reference state are taken into account by the mask function M_i. The complex-valued mask function M [which appears in Eq. (3)] can be written as

$$M(G, \Phi) = Ge^{j\Phi} \tag{4}$$

to account for the gain G of the amplifiers and the phase shift Φ of the phase modulator. In an ideal pulse shaper, the amplitude and phase of the spectral components can be modulated independently. In this case, the optical amplifiers only affect the spectral amplitude and the phase modulators only affect the phase. Therefore, G and Φ are real-valued functions of the control signals in each device channel.

In case of the integrated pulse shaper, the PMs and SOAs do not perform independently and the G and Φ functions are complex. This is due to the fact that applying a reverse bias signal on a PM for tuning the phase, induces some absorption and affects the signal amplitude. On the other hand, changing the biasing current of the SOA affects the phase of the signal. To consider the mutual effect of the PMs and SOAs in case of the integrated device, we define

$$G = g_{\mathrm{SOA}} \times e^{j\varphi_{\mathrm{SOA}}} \tag{5}$$

$$\Phi = \varphi_{\mathrm{PM}} + j\alpha_{\mathrm{PM}}. \tag{6}$$

In Eq. (5), g_{SOA} is the optical gain and φ_{SOA} is the phase effect of the SOA section. In Eq. (6), φ_{PM} is the phase tuning and α_{PM} is the induced loss due to the reverse bias. It is very important for the full calibration to get the information over the performance of individual optical elements as well as the mutual effect of control signals.

The advantage of the calibration method, as described above, is that the functions HR_i and M_i can be measured separately. HR_i and M_i are in general complex valued functions of the optical frequency. Therefore, evaluating these functions in practice requires measurement of the optical amplitude and phase. In the following section, we explain the experimental method which has been used to characterize the frequency response (amplitude and phase) of individual pulse shaper channels, i.e., HR_i. We then express the mask function, i.e., M_i, in terms of the effect of control signals on the amplitude and phase of the optical signal.

4. Experimental Implementation of the Calibration Method

4.1. Measurement of the Channel Response in Reference State

The method that is explained in this section is based on a frequency domain interferometry. In principle, this technique is the basic of the swept-source OCT (Optical Coherence Tomography) [16] and has been applied to characterize different systems [17]–[19]. In case of the integrated pulse shaper which is presented in this paper, we employ the method to characterize the complex transfer function of the device channels.

The schematic illustration of the measurement method is presented in Fig. 2. The setup is configured in the form of a Mach–Zehnder interferometer (MZI). In this setup, the light from an

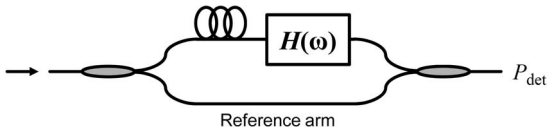

Fig. 2. Schematic drawing of the interferometric setup in the Mach–Zehnder configuration.

optical single frequency laser source is divided between the reference arm and the device. The device arm includes the device under test (DUT) and a time-delay element. The delay element is an additional path length difference between the reference arm and the device arm. The signals of the two arms are then combined and the optical power is recorded. In this method, the frequency of the optical source is tuned and the optical power at the output of the MZI is measured at each frequency. In the interferometric setup, any phase change between the two MZI arms is translated into changes of the optical power, which is easily measured.

The measured optical power P_{det}, can be stated as

$$P_{\text{det}}(\omega) \sim \left|1 + H(\omega)e^{-j\omega\tau}\right|^2 \tag{7}$$

where τ is the time delay in the device arm and $H(\omega)$ is frequency response of the DUT. By applying an inverse Fourier transform, the measured optical power in the time domain can be expressed as

$$p_{\text{det}}(t) \sim \delta(t) + h(t) \otimes h^*(-t) + h(t-\tau) + h^*(-(t+\tau)) \tag{8}$$

where $\delta(\text{t})$ is the Dirac delta, the symbol * is the complex conjugate and $\otimes$ is the convolution operation.

In Eq. (8), the term $h(\text{t}-\tau)$, i.e., the retarded impulse response of the DUT, is isolated in time provided that $h(t)$ corresponds to a causal system, has a finite duration in time and a proper value of τ (larger than the duration of the impulse response) is chosen. Under these conditions, it is possible to filter out the part of the time domain signal $p_{\text{det}}(\text{t})$ which corresponds to the retarded impulse response in the time domain. This is in turn equivalent to finding the system frequency response through a Fourier transform $H(\omega) = \text{F}\{h(t)\}$.

In case of the integrated pulse shaper, the device channels are formed by the AWG channels. We note that here, $h(t)$ corresponds to a physical system which is causal. Furthermore, since the AWG is essentially an FIR (finite impulse response) filter, the duration of $h(t)$ in time is limited. Therefore, the method can be conveniently applied.

Since, the integrated pulse shaper has a reflective geometry, the interferometric setup is easier to realize in the Michelson configuration. This configuration can be realized relatively easily in practice. We have used a cleaved fiber tip to inject light from a single frequency tunable laser to the chip. The reflection of the tip of the fiber could then be used as the reference signal; this makes the length of the reference arm zero. The loss in the optical coupling from the fiber to the chip and back is approximately 10 dB higher compared to a lensed fiber coupling, but the signal strength of the return signal is sufficiently strong to obtain a clear interferogram. Furthermore, the required time delay of the device arm corresponds to the total path length (double pass) of the chip.

As it was described in the previous section, the proposed calibration procedure requires that characterization of the device channels is done separately. The key point which enables individual channel characterization in the current device is that an SOA is included in each channel. If the SOA in the channel is not biased, it effectively absorbs the light in the corresponding channel and hence, there is no return signal to the I/O port. On the other hand, if the SOA is biased to provide enough gain, the signal which goes through the channel and returns to the I/O port where it interferes with the reflected signal from the tip of the cleaved fiber. This forms the required interference pattern which is used to analyze the channel response.

Measuring the complex channel response involves the measurement of the amplitude and phase of the frequency response according to the basic method and corresponding calculations which were described in Section 3. The schematic illustration of the measurement setup is given in Fig. 3.

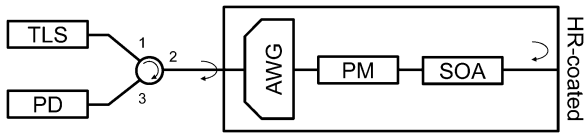

Fig. 3. Schematic illustration of the measurement setup for characterizing the complex transfer function of the individual device channels in the reference state. A cleaved fiber tip is connected to port 2 of the circulator to inject the light to the chip. TLS: tunable laser source, PD: photo detector (optical power meter), HR: high-reflection.

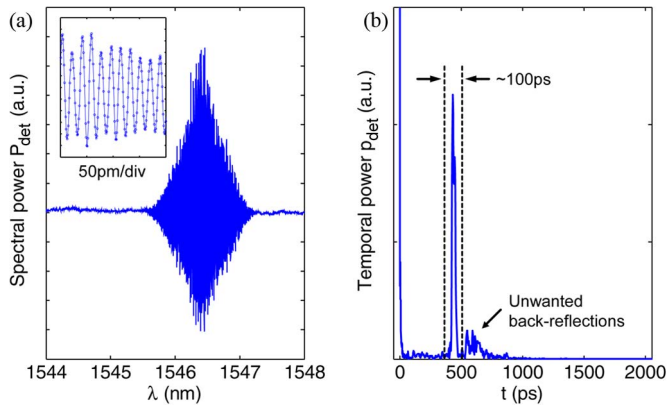

Fig. 4. (a) A typical interferogram which is recorded for channel characterization. The inset is a zoom-in over 0.2nm range to show the number of points per fringe and the spectral resolution. (b) The magnitude of the time-domain representation of the recorded signal. The peak at t $\sim$ 400 ps corresponds to the device channel. The temporal filter which is used to numerically isolate the retarded channel response $h(t)$ is $\sim$100 ps wide.

We have used a continuously tunable laser source to sweep the input signal wavelength and recorded the optical power in steps of 1 pm over a length of several nm to clearly cover the full channel width. The optical power of the source is kept below 3 dBm to make sure nonlinear effects in SOAs, such as self-phase modulation, does not disturb the measurement by violating the LTI system assumption. We measure the interference signal in order to determine the frequency response of each channel. The reference state of control signals is chosen as $V_{PM} = 0$ V and $I_{SOA} = 40$ mA.

A typical measurement result which shows the interference pattern is given in Fig. 4(a). In this figure, the laser source is scanned over the wavelength range $\lambda = 1544 - 1548$ nm and the SOA in channel 10 is biased at $I_{SOA} = 40$ mA. The inset is a focus on the interference fringes and shows that the wavelength step of 1 pm provides sufficient sample points to resolve the fringes properly.

The magnitude of the inverse Fourier transform of the measured optical power is given in Fig. 4(b). The signal which passes through the chip is delayed by approximately 400 ps. This corresponds to the total travel time through the device length (double pass) which was denoted as the term τ in Eq. (7) and Eq. (8). In Fig. 4(b), the peak that appears at t $\sim$ 400 ps corresponds to the retarded impulse response of the channel, i.e., $h(t - \tau)$ in Eq. (8). The temporal peak is well separated from the other signals and well above the noise floor. The isolated peak in the time domain is then filtered out, as indicated in the inset of Fig. 4(b). The complex frequency response of the channel is then calculated by a Fourier transform, i.e $H(\omega) = F\{h(t)\}$.

The measured transfer function, i.e., peak amplitude normalized to 1 and the spectral phase, of the device channel number 10 at $V_{PM} = 0$ V and $I_{SOA} = 40$ mA is given in Fig. 5. The wavelength dependence of the channel response is caused by the filtering effect of the AWG channel. Therefore, the magnitude of the channel response is a measurement of the transmission of the AWG channels. In order to confirm this, we have measured the power transmission through the

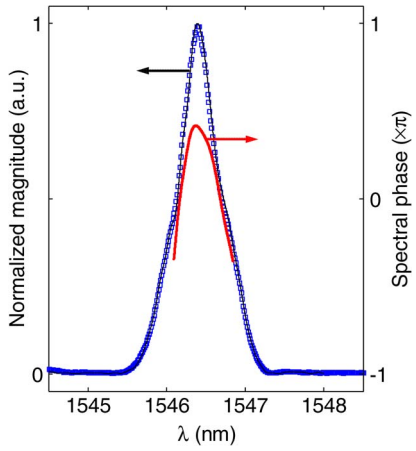

Fig. 5. Frequency response (magnitude normalized to 1 and phase) of channel 10 at the reference state ($I_{SOA} = 40$ mA, $V_{PM} = 0$ V). Blue squares show the transmission spectrum of the AWG channel 10 which is measured separately.

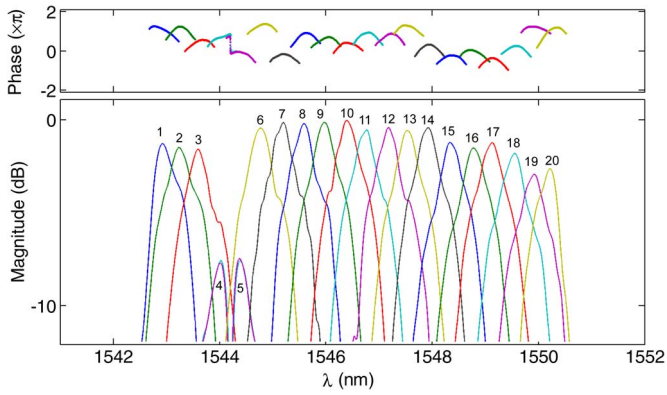

Fig. 6. Individual channel response (magnitude and phase) for the 20 device channels. Channel numbers are indicated on the plot.

AWG channel directly. The AWG channel was characterized by biasing the SOA in channel 10. When the SOA is turned on, it generates amplified spontaneous emission (ASE). The SOA is then used as an on-chip broad-band light source. We have then measured the optical signal at the I/O waveguide using an optical spectrum analyzer. This gives the transmission spectrum of the AWG channel. The measured power transmission spectrum of the AWG channel is presented in Fig. 5 (squares) and it compares very well with the magnitude of the channel response.

Following the same technique, we have measured the complex response of all the individual device channels at the reference state. An overview of all results is given in Fig. 6. The total system response of the shaper in the reference state can be calculated by a complex summation of these measured frequency responses. It is seen from Fig. 6 that the frequency response for the channels 4 and 5 appear to be different from the other channels. This is caused by a short circuit problem between the contacts on the SOAs in those two channels which made that these SOAs could not be biased individually. Furthermore increasing the bias current on these two SOAs did not increase the gain in the channels. We were not able to resolve this issue.

The spectral phase response curves of the channels are quite similar. The shape can be approximated by a quadratic relation over the width of the channel. The spectral phase response determines the channel dispersion which is an important issue for pulse shaper devices. The phase

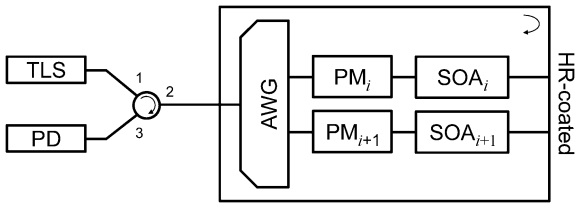

Fig. 7. Schematic illustration of the measurement technique which is used to evaluate the effect of control signals. Two neighboring device arms form an on-chip Michelson interferometer structure. An AR-coated lensed fiber tip is connected to port 2 of the circulator to inject the light to the chip.

offset values vary randomly over the channels. It reflects the fact that the optical path length of each channel is not controlled down to the sub-wavelength level in the manufacturing.

4.2. Effect of Control Signals

Knowledge of the performance of tuning elements, i.e., the effect of control signals on the phase and amplitude of the optical signal, is required for proper operation of the pulse shaper. For open-loop operation of the pulse shaper, it is particularly important that the device components are characterized on-chip. In Section 3, we presented the mathematical description of the mask function which includes the effect of control signals on the PMs and SOAs. The method that has been used to characterize the effect of PMs and SOAs is described in this section.

The width of the AWG channels in our device has been designed to be equal to the channel spacing, i.e., 50 GHz. Therefore, the AWG channels overlap at the 3 dB width. If a laser light signal is injected into the device, such that its wavelength is spectrally located in between two neighboring channels, the signal is effectively split between the two adjacent channels. The signal then travels in the waveguides, through corresponding PMs and SOAs. If both SOAs are switched on at the same time, the optical signals of the two neighboring channels pass through to return to the I/O waveguide. This structure forms a Michelson interferometer where the two adjacent channels form the two arms of the interferometer. This Michelson interferometer structure is formed on the chip and therefore it provides a very stable interferometer structure to measure the effect of control signals on an optical signal which is passing through the structure. The on-chip Michelson interferometer is schematically illustrated in Fig. 7. This is the basis for characterizing the relative phase effect of PMS and SOAs.

4.2.1. PM: Phase Tuning and Induced Excess Loss

The contribution of the effect of PMs to the mask function is mathematically described as in Eq. (6). This includes a phase shift as a function of the applied voltage, as well as possible excess loss which occurs due to absorption of the light in presence of the external electric field. In order to characterize the PMs, we have followed the measurement technique which was described above and illustrated in Fig. 7. The SOAs in two neighboring channels are forward biased at the reference state, i.e., $I_{SOA} = 40$ mA. The voltage bias on one of the PMs is kept constant at $V_{PM} = 0$ V, whereas the bias voltage on the other PM is scanned. The output power is measured for each value of the voltage. Single frequency laser light is injected to the chip using an AR-coated lensed fiber tip to minimize back reflections from the tip of the fiber. A circulator is used to separate the input/output directions outside the chip. The result is an interferogram which we have used to extract the PM parameters.

A typical measurement result is given in Fig. 8. The interference pattern is fitted to an analytical expression which is given by

$$P_{\text{int}} = f_0 + f_1^2 + [f_2 I(\text{V})]^2 + 2 f_1 f_2 I(\text{V}) \cos(\varphi(\text{V})) \tag{9}$$

in which P_{int} is the measured interferogram (power), f_0 is the background signal and f_1 is the electric field amplitude in the interferometer arm with the PM that is not scanned. The signal electric field amplitude in the arm in which the PM bias is scanned is given by its maximum value f_2 and a

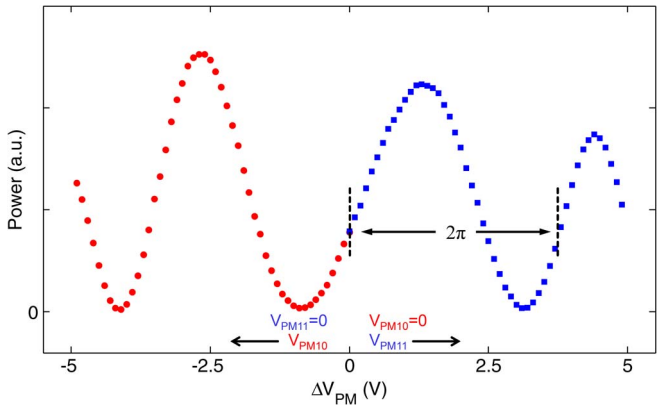

Fig. 8. A typical interferogram which is used to measure the parameters of the PMs. In this measurement, device channels 10 (red circles) and 11 (blue squares) are biased together. The effect of additional loss of the PM at higher bias voltage is seen as the reduced modulation depth of the interference pattern.

function $I(\mathrm{V})$, which describes the induced voltage dependent loss in the field. The voltage dependent loss in one arm of the Michelson interferometer causes an imbalance between the signal amplitudes in the arms and reduces the modulation depth of the interferogram with increasing voltage. This effect is clearly seen in Fig. 6 for voltage values near 5 V. We have used an empirical relation to express the excess loss as a function of the bias voltage as

$$I(\mathrm{V}) = 1 - f_3 \mathrm{V}^3. \tag{10}$$

The phase tuning function, $\varphi(\mathrm{V})$, is phenomenologically expressed by a second order polynomial as

$$\varphi(\mathrm{V}) = f_4 + f_5 \mathrm{V} + f_6 \mathrm{V}^2 \tag{11}$$

in which f_4 is the phase offset between the two neighboring arms, f_5 and f_6 are the linear and quadratic phase shift terms. The quadratic phase term is mainly attributed to the quantum-confined Stark effect.

Eqs. (9)–(11) include seven fitting parameters (f_0 to f_6) in total. The nonlinear curve fitting problem is solved in the least-squares sense. We first present the results obtained for the phase tuning curves $\varphi(\mathrm{V})$. These phase tuning data have been measured for the PMs in the different channels of the pulse shaper. The data are recorded at wavelengths over one FSR of the AWG in the device around 1529 nm.

The linear and quadratic terms of the fitted curves are given in Fig. 9. As mentioned before the SOA sections in channels 4 and 5 are short circuited and cannot be controlled independently. The transmitted power through these channels at the reference state is 10 dB lower than the neighboring channels. Therefore, we were not able to measure the PM performance in these two channels. The PMs in channels 1, 19, and 20 have not been measured. The data points corresponding to these channels are missing in Fig. 9. The tuning curves for the PMs are fairly consistent below 4 V. The required voltage for a 2π phase shift is $\sim$3.7 V on average. At this value of the bias voltage, the amount of phase shift for all the PMs is $2\pi \pm 0.25\pi$. This is shown in Fig. 10.

The values of the parameter f_3 give the voltage dependent loss of the PMs as in Eq. (10). From the fit values, the voltage dependent power losses for the PMs were calculated. These results are presented in Fig. 11. The excess loss of the PM in channel 9 was also measured in an independent way. This result is given in Fig. 11 (red squares) for comparison. This loss curve is obtained by measuring the ASE power of the SOA in channel 9. The SOA is biased at $\mathrm{I_{SOA}} = 40$ mA and the fiber-coupled output ASE power is measured. When the reverse bias on the PM in channel 9 is increased, the measured ASE power reduces due to the absorption in the PM. The difference in the

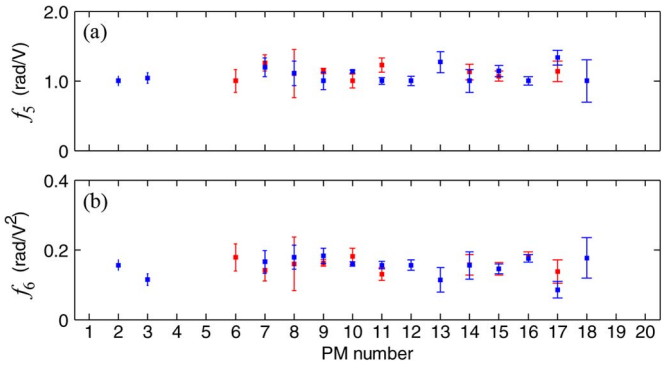

Fig. 9. (a) Liner and (b) quadratic phase shift parameters with the 95% prediction confidence intervals. The red and blue colors indicate separate measurements. Measurement data for PMs in channels 1, 4, 5, 19, 20 are not available.

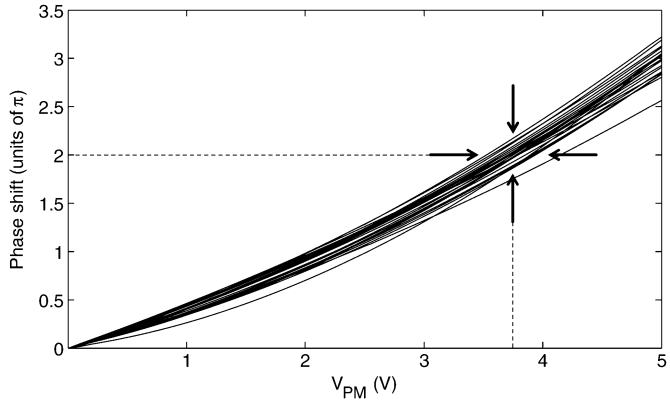

Fig. 10. Measured phase tuning curves of the PMs. The required voltage for a 2π phase shift (double pass) is $\sim$3.7 V on average. At this value of the bias voltage, the amount of phase shift for all the PMs is $2\pi \pm 0.25\pi$.

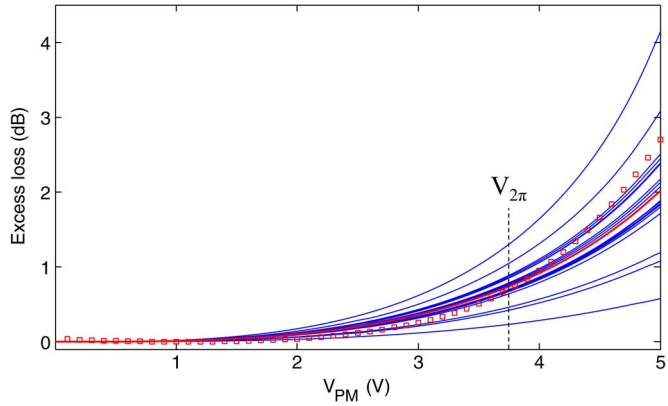

Fig. 11. Voltage dependent loss of the PMs calculated based on the fitted parameters (solid blue). The calculated curve for channel 9 is indicated as a thick red line. The excess power loss of the same PM which is measured independently (red squares) is given for comparison.

measured power level is interpreted as the excess loss of the PM section in presence of the reverse bias. This result shows that for operation of the PMs below 4 V, the voltage dependent loss is described sufficiently accurate using Eq. (10).

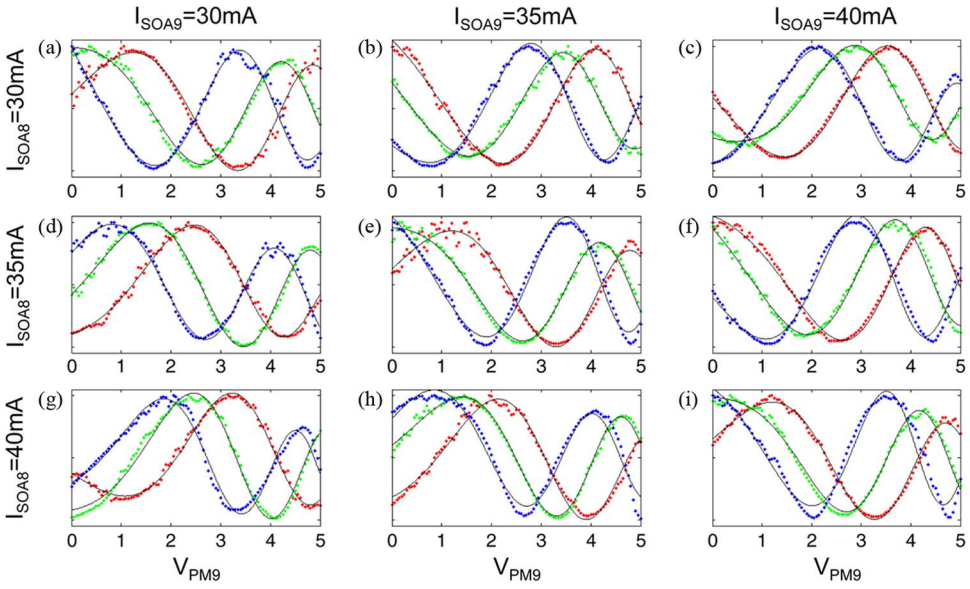

Fig. 12. Measured interferograms (dots) with the device channels 8 and 9. Bias voltage value in channel 8 is kept constant at $V_{PM8} = 0$ V and V_{PM9} is scanned. The fitted curves are shown as solid black lines. $\lambda = 1551.7$ nm (red), $\lambda = 1543.8$ nm (green) and $\lambda = 1536.0$ nm (blue).

The measured parameters define the PM performance that is described Eq. (6) in terms of the control voltage on the PM. The PM loss factor, α_{PM} in Eq. (6), can then be calculated as

$$\alpha_{PM} = \ln(I(V)) = \ln\left(1 - f_3 V_{PM}^3\right) \tag{12}$$

where ln is the natural logarithm function. The phase shift, φ_{PM} in Eq. (6), is directly linked to the fitted parameters (f_5 and f_6) through

$$\varphi_{PM} = f_5 V_{PM} + f_6 V_{PM}^2. \tag{13}$$

We note that the measured data for the PMs are obtained at different wavelengths within one FSR of the device. The fitted parameters for different PMs do not show a clear wavelength dependence trend over the limited range ~1526–1532 nm. The PM parameters are in principle wavelength dependent for two reasons. The PM voltage changes the phase of the light by changing the optical path length through a change in refractive index. This gives a λ^{-1} dependency. The refractive index also changes with wavelength due to material dispersion and the effect of proximity to the band-gap wavelength of the MQW core. However the differences between the properties of the PMs appear larger than the wavelength dependence over the limited wavelength range.

To have an indication of the wavelength dependence of the phase tuning parameters, we present measurement results obtained with scanning the PM in channel 9 for three different wavelengths. These are three different orders of the AWG transmission spectrum that connect to channel 9. In these measurements the SOAs in the channels 8 and 9 are both biased. The PM voltage in channel 8 is kept at $V_{PM} = 0$ V. The same measurement and fitting method as described in the preceding paragraphs was used to find the PM parameters at different wavelengths. In this case, we have repeated the measurements at different values of SOA bias, i.e., $I_{SOA} = 30$ mA, 35 mA, and 40 mA. This gives a set of 9 different measurements. The measured data are presented in Fig. 12. The recorded data for each wavelength are indicated by a different color and the SOA bias values are given in the figure. The nine interference patterns for each wavelength presented in Fig. 12 were fitted simultaneously to determine the PM parameters, at that wavelength, to the expressions given in Eq. (9)–(11).

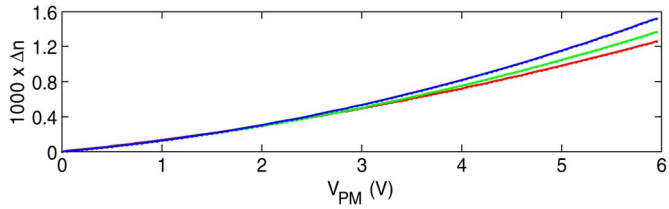

Fig. 13. Voltage dependent change of the refractive index calculated based on the measurement results given in Fig. 12 at $\lambda = 1551.7$ nm (red), $\lambda = 1543.8$ nm (green) and $\lambda = 1536.0$ nm (blue).

The PM parameters which govern the voltage dependent phase shift were measured at the three wavelengths. The voltage dependent phase shift can be expressed in terms of the voltage dependent change of the refractive index of the PM section according to

$$\Delta n = \frac{\varphi_{\mathrm{PM}}}{2\pi}\frac{\lambda}{2L_{\mathrm{PM}}} \tag{14}$$

in which $2L_{\mathrm{PM}}$ is the double-pass length of the PM section. The calculated Δn versus the voltage is given in Fig. 13.

The term f_4 which appears in the relation between phase and voltage in Eq. (11) is a constant phase term that is not included in the voltage dependent phase shift in Eq. (13) which goes back in the mask function M. In our measurements, this term represents the phase difference between the arms of the Michelson interferometer when both PMs are biased at $V_{\mathrm{PM}} = 0$.

There are three main conclusions regarding the phase offset between the channels which follow from the plots of Fig. 12. First, if a single plot with the interferograms at the three wavelengths is considered, we see that the phase offsets (at $V_{\mathrm{PM}} = 0$) are different for the different wavelengths. This means that the phase offset is wavelength dependent. Second, the phase offset also depends on the relative bias level of the SOAs. This can be seen by considering the off-diagonal plots [Fig. 12(b)–(d) and (f)–(h)] at each wavelength. This is a measure of the effect of the SOA on the phase of the signal in the channel.

The third conclusion is drawn by considering the diagonal plots, i.e., Fig. 12(a), (e) and (i). In this case, we observe that the phase offset remains the same when the SOA bias levels in the two arms are the same. This shows that the amount of induced phase change by an SOA bias change is, within our measurement accuracy, the same for both SOAs. The effect of SOA bias on the phase of the optical signal will be discussed in detail in the following subsection. In our calibration scheme, the phase offset between the channels appears as the difference in the phase of the frequency response of the channels. This is taken into account in the reference state, as described in Section 3.

4.2.2. SOA: Optical Gain and Induced Phase Change

For the SOAs, the change from the reference point in optical gain and the change in phase as a function of injection current need to be determined. We define the relative gain, g_{r}, as

$$g_{\mathrm{r}} = \frac{g}{g_{ref}} \tag{15}$$

where g is the optical gain at any bias condition, i.e., any value of I_{SOA}, and g_{ref} is the optical gain at the reference bias level. The change in optical gain can be measured in a straightforward way. The light from a single frequency continuous wave laser source is tuned to a particular device channel, is kept at a constant power level and is injected into the device via a circulator. The returning output power from the shaper is then measured as a function of the current in the SOA of the addressed channel. The ratio of the measured output power to the measured output power at the reference bias current is the value of g_{r}. The reference state is defined at $I_{\mathrm{SOA}} = 40$ mA. The measured values for g_{r} as a function of current are given in Fig. 14 for channels 8, 9 and 10. As can be seen, the gain

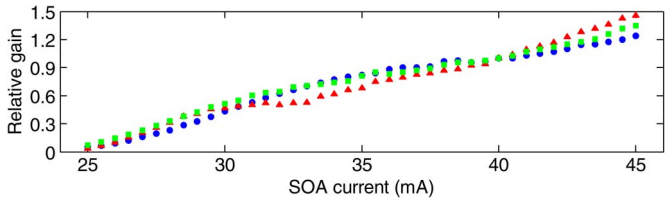

Fig. 14. Relative gain measured with SOAs in the device channels 8 (green squares), 9 (blue circles) and 10 (red triangles).

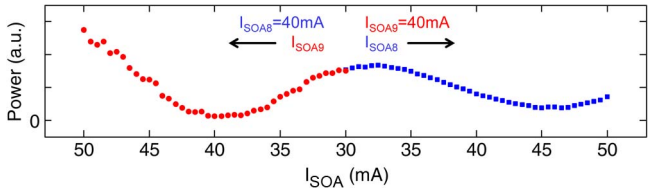

Fig. 15. A typical interferogram which is used to measure the phase effect of the SOAs. In this measurement, device channels 8 (blue squares) and 9 (red circles) are biased together.

cannot be increased much above the reference state. This is limited by reflections in the chip. The minimum measurable relative gain is determined by the ASE from the amplifier and the total device losses. In Eq. (5), the term g_{SOA} is equal to the square root of the relative gain.

It appeared that the amplifier behavior with respect to the relative gain was sufficiently uniform (better than 5% of the average above 35 mA and within 20% overall) to have the same parameters for all amplifiers in the masking function. It can be concluded that useful range for the SOA bias current is 25 to 45 mA.

As well as causing a change in optical gain, a change in injection current of the SOA affects the phase of the light in the channel. This effect is due to the change in carrier density with the changing injection current and the change of the temperature in the SOA. Since our pulse shaper is operated electrically in DC mode, we cannot separate between the two origins. It is possible to measure the overall effect of the SOA bias on the phase of the optical signal. This effect was evaluated by using the on-chip Michelson interferometer structure that was used to characterize the phase tuning performance of the PMs. However, in this case the PM voltage is kept constant at $V_{PM} = 0$ and the SOA current is scanned. The measured optical power then provides interference patterns according to phase changes induced by I_{SOA}. The interference patterns are then analyzed to obtain the phase difference between the arms versus the SOA bias current. For the 30–50 mA range of applied current in Fig. 15, the induced phase change is linear with the current and can be expressed as

$$\varphi_{SOA} = f_7 \times \Delta I_{SOA} \tag{16}$$

in which f_7 is the fit parameter which is determined to be 0.2704 ± 0.004, ΔI_{SOA} is the difference between the operating current of the SOA and I_{SOA} at the reference state, i.e., $I_{SOA} = 40$ mA. The term φ_{SOA} directly links to the function G that is defined as in Eq. (7). This value was used for all the channels in the calibration.

5. Verification of the Channel Characterization Method

In this section we round off the work on the calibration of the pulse shaper with a measurement to confirm the interferometric method used to measure the reference states and a measurement to show that the pulse shaper indeed behaves as a linear system and that the system response is correctly predicted using the reference state and mask function.

5.1. Verification of the Channel Characterization Method—SIMBA Technique

We first verify the interferometric method which is used to measure the frequency response of the device. In this section, we show how the SIMBA (Spectral Interferometry using Minimum-phase Based Algorithm) method can be used to characterize a device channel. We then compare the result obtained with the SIMBA method and the one which is achieved by interferometric technique. In this context, the SIMBA method is of particular interest because it can be used to retrieve the spectral phase response of the device channel. In Section 4.1 (Fig. 5), it was shown that the amplitude of the channel response which is measured by the interferometric method, compares very well with the shape of the AWG channel shape. In this section, the capability of the method to retrieve the spectral phase is verified using the SIMBA method.

The SIMBA method [20] is a measurement technique which can be used for the complete characterization of optical pulses. The SIMBA method involves measuring the power spectrum of a sequence of optical pulses which consists of a dummy pulse and the target pulse, i.e., the optical pulse which is to be characterized. According to the theory behind the SIMBA method, if the dummy pulse is (close to) a minimum phase signal, the spectral amplitude and phase of the target pulse can be retrieved by merely measuring the power spectrum.

SIMBA is a powerful option to verify our calibration method since it is able to characterize the optical pulse which passes through the pulse shaper. Furthermore, it does not require a high optical power level and is able to operate the wavelengths of our interest. In our SIMBA setup, the optical pulse source is an FSL1010 fiber laser source which generates 150 fs optical pulses at 80 MHz repetition frequency. The central wavelength is around 1560 nm. The optical pulse is sent through an optical circulator and a cleaved fiber tip is used to inject the pulses to the pulse shaper. A part of the signal is reflected at the tip of the fiber. This signal which is a replica of the short input pulse is the dummy (reference) pulse for SIMBA measurements. A part of the signal which is coupled to the chip passes through the operating channels and returns to the I/O waveguide. This signal is the target pulse which characterizes the channel response. The sequence of the dummy and target pulses is then measured by an APEX high resolution (20 MHz) optical spectrum analyzer to resolve spectral features, the interference between the pulses. The recorded spectrum is then analyzed by an iterative mathematical algorithm to retrieve spectral amplitude and phase of the target pulse.

The key point here lies in the fact that, if the input pulse has sufficiently short time duration such that it could be approximated by an impulse signal $\delta(t)$, the output pulse will, by definition, be the system impulse response $h(t)$. Therefore, by retrieving the amplitude and phase of the output signal we achieve the system frequency response. In our setup the input pulse is close to an impulse signal; hence, the target pulse approximates the frequency response of the channel.

We set the control signals in channel 10 at the reference state, i.e., $I_{SOA} = 40$ mA and $V_{PM} = 0$ V. The measurement result obtained with the SIMBA method is given in Fig. 16(a). The frequency response of the channel as measured with the interferometric method is given in Fig. 16(b) for comparison. The spectral magnitude and the spectral phase of the channel match for both methods very well. This demonstrates that the measurement method that is presented in Section 3 is reliable.

5.2. Test Measurement of the Control Signal Calibration

To demonstration that our approach on how to control the pulse shaper is working correctly we performed a measurement along the steps listed below. For convenience, we have considered only channels 9, 10, and 11.

1. First we bias the SOA in the channels, one at a time, and measure the individual channel response at $I_{SOA} = 40$ mA and $V_{PM} = 0$ V using the interferometric method. This is defined as the channel response at the reference state.
2. Next, we bias the three channels together and measure the total response using the same method. The result is shown in Fig. 17(a). Now we calculate the complex summation of the three channels at the reference state and compare it with the measured result of the three channels together. As indicated in Fig. 17(a), we observe that the measured total response matches very well with the summation of individual channel responses. This verifies the

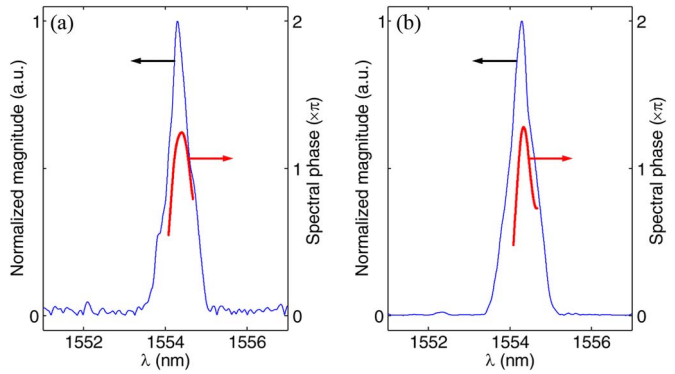

Fig. 16. Complex frequency response (spectral amplitude and phase) of the device channel number 10, measured with (a) the SIMBA method, and (b) the interferometric method. The results are obtained at the reference state $I_{SOA} = 40$ mA, $V_{PM} = 0$ V.

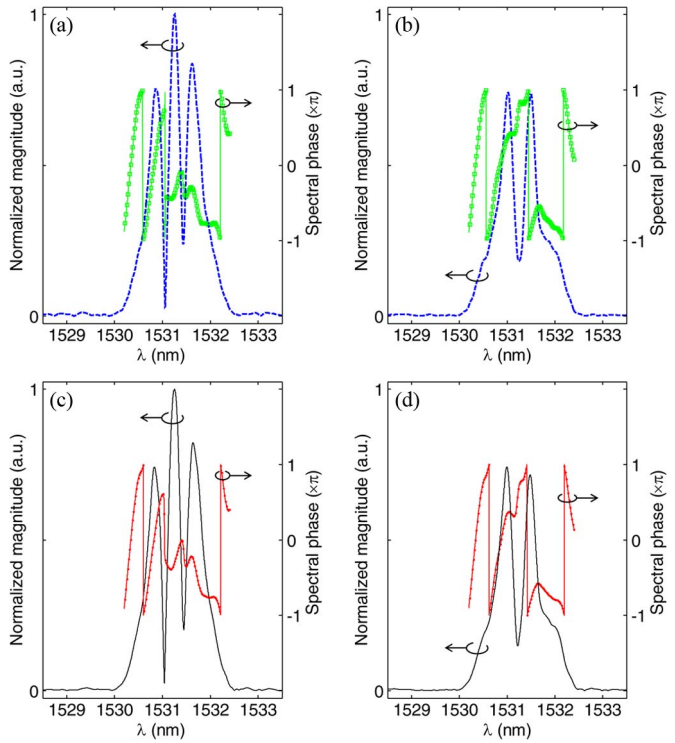

Fig. 17. Normalized amplitude and spectral phase of the system response when the three device channels 9, 10 and 11 are considered. The (a) calculated and (c) measured amplitude and phase of the system response with the three device channels being switched on at the same time at $I_{SOA9,10,11} = 40$ mA and $V_{PM9,10,11} = 0$ V. The (b) calculated and (d) measured system response with channels 9 and 11 at the reference state, $I_{SOA10} = 40$ mA and $V_{PM10} = 2.3$ V.

assumption that the total channel response is a linear summation of individual channel responses.

3. Then we consider the effect of a control signal. For instance, we apply a reverse bias on the PM in channel 10 of $V_{PM10} = 2.3$ V. This corresponds to a π phase change in channel 10. We then put this phase change in the mask function and multiply it with the reference state response of channel 10 to calculate the response of channel 10 at this operating point [Eq. (3)]. The total system response is again calculated by a summation of the channel responses

[Eq. (2)]. The calculated result is shown in Fig. 17(b). The total system response with the channels 9 and 11 at the reference state and $V_{PM10} = 2.3$ V is measured separately and given for comparison. The agreement between the measured and calculated results is clear and confirms the proposed calibration method.

6. Conclusion

We have presented a theoretical description of an InP monolithically integrated optical pulse shaper and proposed a method for calibration of the device. In our approach, the total frequency response of the device is calculated as a summation of the frequency response of the device channels. The frequency response of the individual channels is described by the channel response in a reference state of the control signals and a separate mask function which considers the effect of a change of the control signals from the reference state. The channel response in the reference state and the mask functions are determined experimentally.

The measurement method that has been used to characterize the complex (amplitude and phase) response of the channels was verified using the SIMBA technique. Test measurements are presented as well to show that the system response is correctly predicted using the presented calibration method.

The results of the device channel characterization show that the frequency response functions of the channels are quite similar. The amplitude response follows the AWG channel passband, which is as expected. The spectral phase response of the channels is mainly dominated by the AWG channel response which in turn is due to imaging errors in the free propagation region of the AWG (mainly related to imperfect focusing of the star coupler) and amplitude/phase errors in the array of waveguides. We note that although the current device includes a relatively large length of optical waveguide ($\sim$2 cm double pass) in each channel, the effect of the waveguide dispersion is negligible.

The spectral phase response determines the channel dispersion which is an important issue for pulse shaper devices. The non-zero channel dispersion limits the performance of the optical pulse shaper in the conventional group-of-lines pulse shaping regime. This is due to the fact that the spectral amplitude/phase of the frequency components which fall within a single device channel cannot be individually controlled. In the line-by-line pulse shaping regime, the channel dispersion does not affect the device performance in this way. However, the frequency dependence of the phase response means that the instabilities in the input laser mode frequencies translate into instabilities in the output pulse shape. Specific requirements on the pulse shape properties in different application can therefore lead to stringent frequency stability requirements of the laser source. In the current device, the shape of spectral phase can be approximated by a quadratic $(-16\ \text{ps}^2)$ relation over the 10 dB-width of the channel. This means that a change in the frequency of an incident spectral line is of 10 GHz leads to $\sim 0.02\pi$ phase change.

References

[1] A. M. Weiner, "Ultrafast optical pulse shaping: A tutorial review," *Opt. Commun.*, vol. 284, no. 15, pp. 3669–3692, Jul. 2011.
[2] H. Tsuda, K. Okamoto, T. Ishii, Y. Inoue, H. Takenouchi, and T. Kurokawa, "Second- and third-order dispersion compensator using a high-resolution arrayed-waveguide grating," *IEEE Photon. Technol. Lett.*, vol. 11, no. 5, pp. 569–571, May 1999.
[3] H. Tsuda, H. Takenouchi, T. Ishii, K. Okamoto, T. Goh, K. Sato, A. Hirano, T. Kurokawa, and C. Amano, "Spectral encoding and decoding of 10 Gbit/s femtosecond pulses using high resolution arrayed-waveguide grating," *Electron. Lett.*, vol. 35, no. 14, pp. 1186–1188, Jul. 1999.
[4] H. Takenouchi and T. Goh, "2/spl times/40-channel dispersion-slope compensator for 40-Gbit/s WDM transmission systems covering entire C- and L-bands," in *Proc. Opt. Fiber Commun. Conf. Exhib.*, 2001, pp. 2–4.
[5] K. Mandai, T. Suzuki, H. Tsuda, T. Kurokawa, and T. Kawanishi, "Arbitrary optical short pulse generator using a high-resolution arrayed-waveguide grating," in *Proc. IEEE Intl. Top. Meet. Microw. Photon. (IEEE Cat. No.04EX859)*, Oct. 2004, pp. 107–110.
[6] K. Takiguchi, K. Okamoto, T. Kominato, H. Takahashi, and T. Shibata, "Flexible pulse waveform generation using silica-waveguide-based spectrum synthesis circuit," *Electron. Lett.*, vol. 40, no. 9, pp. 537–538, Apr. 2004.

[7] K. Okamoto, T. Kominato, H. Yamada, and T. Goh, "Fabrication of frequency spectrum synthesiser consisting of arrayed-waveguide grating pair and thermo-optic amplitude and phase controllers," *Electron. Lett.*, vol. 35, no. 9, pp. 733–734, Apr. 1999.
[8] R. P. Scott, N. K. Fontaine, J. Cao, K. Okamoto, B. H. Kolner, J. P. Heritage, and S. J. Ben Yoo, "High-fidelity line-by-line optical waveform generation and complete characterization using FROG," *Opt. Exp.*, vol. 15, no. 16, pp. 9977–9988, Aug. 2007.
[9] N. K. Fontaine, R. P. Scott, J. Cao, A. Karalar, W. Jiang, K. Okamoto, J. P. Heritage, B. H. Kolner, and S. J. Yoo, "32 Phase X 32 amplitude optical arbitrary waveform generation," *Opt. Lett.*, vol. 32, no. 7, pp. 865–867, Apr. 2007.
[10] M. J. R. Heck, P. Munoz, B. W. Tilma, E. A. J. M. Bente, Y. Barbarin, Y.-S. Oei, R. Notzel, and M. K. Smit, "Design, fabrication and characterization of an InP-based tunable integrated optical pulse shaper," *IEEE J. Quantum Electron.*, vol. 44, no. 4, pp. 370–377, Apr. 2008.
[11] N. K. Fontaine, R. P. Scott, and S. J. B. Yoo, "Dynamic optical arbitrary waveform generation and detection in InP photonic integrated circuits for Tb/s optical communications," *Opt. Commun.*, vol. 284, no. 15, pp. 3693–3705, Jul. 2011.
[12] S. Tahvili, S. Latkowski, B. Smalbrugge, X. J. M. Leijtens, P. J. Williams, M. J. Wale, J. Parra-Cetina, R. Maldonado-Basilio, P. Landais, M. K. Smit, and E. A. J. M. Bente, "InP-based integrated optical pulse shaper: Demonstration of chirp compensation," *IEEE Photon. Technol. Lett.*, vol. 25, no. 5, pp. 450–453, Mar. 2013.
[13] M. Smit, X. Leijtens, E. Bente, J. van der Tol, H. Ambrosius, D. Robbins, M. Wale, N. Grote, and M. Schell, "Generic foundry model for InP-based photonics," *IET Optoelectron.*, vol. 5, no. 5, pp. 187–194, Oct. 2011.
[14] European manufacturing platform for photonic integrated circuits. [Online]. Available: http://europic.jeppix.eu/
[15] X. J. M. Leijtens, B. Kuhlow, and M. K. Smit, "Arrayed waveguide gratings," in *Wavelength Filters in Fiber Optics*, H. Venghau, Ed. Berlin, Germany: Springer-Verlag, 2006, pp. 125–187.
[16] A. F. Fercher, W. Drexler, C. K. Hitzenberger, and T. Lasser, "Optical coherence tomography—principles and applications," vol. 66, no. 2, pp. 239–303, Feb. 2003.
[17] M. Froggatt, T. Erdogan, J. Moore, and S. Shenk, "Optical frequency domain characterization (OFDC) of dispersion in optical fiber Bragg gratings," *Trends Opt. Photon.*, vol. 33, pp. 176–178, 1999.
[18] B. J. Soller, D. K. Gifford, M. S. Wolfe, and M. E. Froggatt, "High resolution optical frequency domain reflectometry for characterization of components and assemblies," *Opt. Exp.*, vol. 13, no. 2, pp. 666–674, Jan. 2005.
[19] E. D. Moore and R. R. McLeod, "Correction of sampling errors due to laser tuning rate fluctuations in swept-wavelength interferometry," *Opt. Exp.*, vol. 16, no. 17, pp. 13139–13149, Aug. 2008.
[20] A. Ozcan, *Non-Destructive Optical Characterization Tools: Spectral Interferometry Using Minimum-Phase Functions.* Saarbrucken, Germany: VDM Verlag Dr. Mueller e.K., 2008, p. 272.